CrystEngComm

HIGHLIGHT

View Article Online
View Journal | View Issue

Cite this: *CrystEngComm*, 2022, **24**, 5663

Solid solutions based on $BaZn_2Si_2O_7$ with thermal expansions from negative to highly positive – a review

Christian Thieme *[a] and Christian Rüssel [b]

The compound $BaZn_2Si_2O_7$ shows a transition from a monoclinic low temperature phase to an orthorhombic high temperature phase at 280 °C which is accompanied by an increase in the volume of 3.3%. The temperature of the phase transition can be shifted to higher temperature by a replacement of Zn^{2+} by Mg^{2+} or the divalent transition metal cations, Mn^{2+}, Co^{2+}, Ni^{2+} or Cu^{2+} as well as by the replacement of Si^{4+} by Ge^{4+}. By contrast, the replacement of Ba^{2+} by Sr^{2+} leads to the shift of the phase transition to lower temperatures. The coefficient of thermal expansion of the low temperature phase is exceptionally high and in the range from 10 to 15 10^{-6} K^{-1}, while that of the high temperature phase is small or even negative. The reason of the latter effect is a rotation of bridged ZnO_4 tetrahedra in opposite directions. This results in a strongly negative thermal expansion of the *b*-axis, while the expansion of the *a*- and *c*-axes are positive. Although melts of the stoichiometric compounds do not build a continuous network, glass formation can be achieved by the addition nucleation inhibitors, such as ZrO_2, Al_2O_3 or La_2O_3 or an excess of SiO_2. The quenched glasses crystallize at the surface while bulk crystallization is not observed. This changes if noble metals or higher concentrations of ZrO_2, WO_3 or P_2O_5 are added to the glass, then also bulk crystallization is possible. Homogeneously crystallized glass ceramics can also be obtained, by sinter crystallization of powdered glass or using sol–gel derived crystalline powders. Adjusting the composition of the respective solid solutions enables to tailor the coefficient of thermal expansion from negative to highly positive values.

Received 16th May 2022,
Accepted 18th July 2022

DOI: 10.1039/d2ce00667g

rsc.li/crystengcomm

1. Introduction

The compound $BaZn_2Si_2O_7$ shows a transition from a low to a high temperature phase at around 280 °C, accompanied by a steep increase in volume of 3.3%.[1] The low temperature phase shows a high coefficient of thermal expansion (CTE), which is in the range from 10–15 × 10^{-6} K^{-1}, while the CTE of the high temperature phase is very low or even negative.[2] The stoichiometric composition $BaZn_2Si_2O_7$ does not form a glass, however, the addition of some SiO_2 (or other oxides) leads to glass formation. From such a glass, the $BaZn_2Si_2O_7$ based phases can be crystallised by thermal treatment.[3,4]

During the phase transformation, the crystal structure changes from monoclinic (<280 °C) to orthorhombic (>280 °C). The monoclinic low temperature phase (LT-phase) possesses a high (CTE) of 16 × 10^{-6} K^{-1}, while the CTE of the high temperature phase (HT-phase) is small or even negative.[1] In $BaZn_2Si_2O_7$, a total or partial replacement of Zn^{2+} by other divalent cations shifts the phase transition temperature to higher values.[2,5] This enables the preparation of materials with exceptionally high CTEs, also in the range from room temperature to 1000 °C, which are required for crystallizing glass seals to join metals, *e.g.* for high temperature solid oxide fuel cells (SOFC) or other high temperature reactors.[6–8]

Otherwise, a partial substitution of Ba^{2+} by Sr^{2+} shifts the phase transition temperatures to lower values, even below room temperature.[9] This enables the preparation of materials with a low thermal expansion.[10] Such materials, however, based on lithium aluminosilicates and not on $Ba_{1-x}Sr_xZn_2Si_2O_7$, are nowadays used for a large variety of applications, such as cook top panels, telescope mirrors, furnace windows and various optical devices.[11–13]

Negative thermal expansion at room temperature and higher is an uncommon physical property, since most materials expand with increasing temperature. The most common materials with zero thermal expansion are silicates based on lithium aluminosilicates, such as beta-quartz and beta-eucryptite.[14] These phases can be crystallized from glasses and enable the fabrication of large ceramic

[a] *Fraunhofer-Institut für Mikrostruktur von Werkstoffen und Systemen IMWS, Walter-Hülse-Straße 1, D-06120 Halle (Saale), Germany.*
E-mail: christian.thieme@imws.fraunhofer.de
[b] *Otto-Schott-Institut für Materialforschung, Jena University, Fraunhoferstr. 6, D-07743 Jena, Germany*

specimens, *e.g.* telescope mirror blanks with diameters of several meters.[15] Other phases with negative thermal expansion which can be crystallized from glasses are $MB_2Al_2O_7$ with M = Ba, Ca, Sr.[16–18] Besides, ZrW_2O_8 and materials derived hereof are among the most commonly known negative thermal expansion phases.[19,20] However, they cannot be crystallized from glasses. ZrO_2 as well as WO_3 do not act as glass formers. To achieve glass formations, high quantities of other glass formers such as B_2O_3 or SiO_2 are necessary. If from such glasses, ZrW_2O_8 might be crystallized (although not described in the literature), the high quantities of residual glass phase cannot lead to zero thermal expansion.

In the following, the formation of solid solutions based on $BaZn_2Si_2O_7$ is described. The replacement of Ba^{2+}, Zn^{2+} or Si^{4+} by other ions strongly affects the temperature attributed to the phase transition from the low to the high temperature phase and hence also the CTE. It is further described, how bulk materials based on these solid solutions can be prepared by sintering or by glass crystallization and how the CTE can be tailored.

2. Crystal structure and thermal expansion of pure $BaZn_2Si_2O_7$

The compound $BaZn_2Si_2O_7$ has a high coefficient of thermal expansion up to a temperature of 280 °C. The attributed LT-phase is monoclinic with the space group $C2/c$.[1] Then, a transition to a high temperature phase, with the orthorhombic space group $Ccm2_1$, occurs. The thermal expansion behaviour is shown in Fig. 1. The coefficient of thermal expansion (CTE) of the LT-phase is exceptionally high and in the range of 10–15 × 10^{-6} K^{-1}. The phase transition is accompanied by a steep increase in volume of around 3.3%.[1] The HT-phase has a small or even negative CTE. Fig. 1 shows a comparison of results from dilatometry using a sintered powder compact and high-temperature X-ray powder diffraction (HT-XRD). To plot both data sets on one axis, the volumes from HT-XRD were converted to corresponding changes in length by taking the cube root. The thermal expansion measured by dilatometry and XRD are almost identical below as well as above the phase transition. The height of the volume jump, however, is different. In dilatometric measurements of compressed and sintered powders, the height of this jump cannot be exactly reproduced because the compact sample is damaged during phase transition.

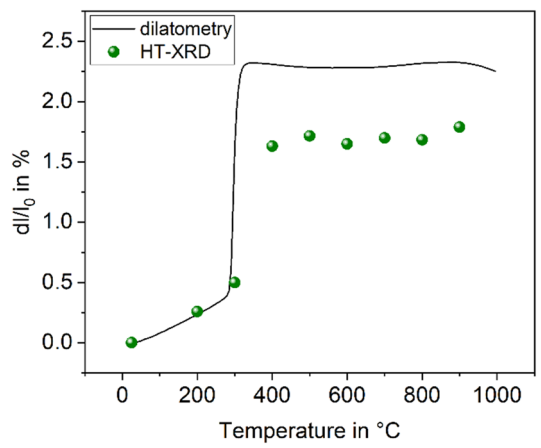

Fig. 1 Thermal expansion of $BaZn_2Si_2O_7$. Redrawn based on ref. 5.

Fig. 2 shows the crystal structures of LT- and HT-phase, respectively. Both structures are fairly similar: silicon and zinc are both fourfold coordinated and, in both cases, two silicon tetrahedra are bridged by oxygen. ZnO_4-tetrahedra form chains aligned along the crystallographic *c*-axis. The Ba^{2+} ions are located in channels and possess a quadratic pyramidal coordination where the Ba–O bond length of the apex is notably longer. Please note that the monoclinic and the orthorhombic unit cells are defined in a different manner and hence it is favourable to compare different planes and directions. For all subsequent descriptions, the crystallographic directions have been renamed. This facilitates to compare the HT- and LT-phases as well as their crystallographic directions. The directions were defined according to Fig. 2.

In Fig. 3, the changes in the lattice constants of both the low and the high temperature phase are shown. From room temperature to 280 °C, the lengths of *a*- and *b*-axes increase strongly, while the CTE of the *c*-axis is smaller. The phase transition is clearly seen and accompanied by an increase of the *a*- and *b*-axes by 1.3 and 3.6%, respectively, while the *c*-axis contracts by around 1.4%. More notably is the behaviour above the phase transition temperature: while the

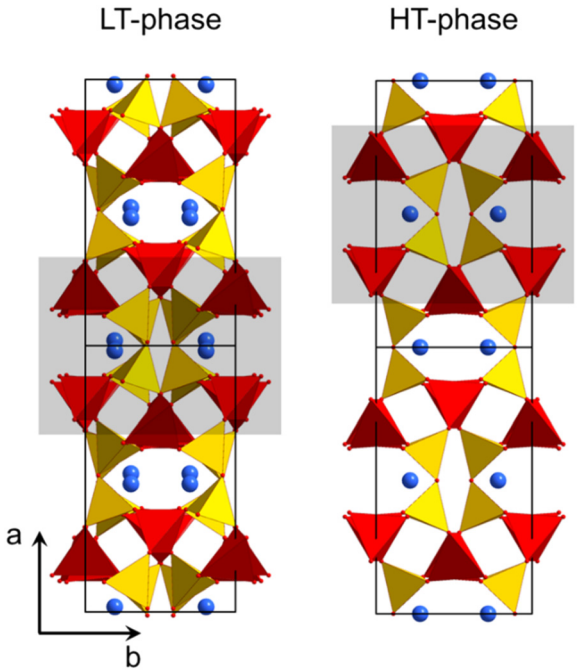

Fig. 2 Crystal structure of LT- and HT-$BaZn_2Si_2O_7$.[1,21] The grey rectangles mark similar structural units, which convert into each other during phase transition.

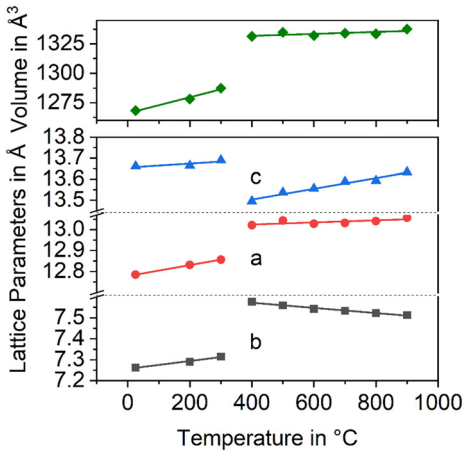

Fig. 3 Lattice constants of $BaZn_2Si_2O_7$ as a function of temperature. Data taken from ref. 2.

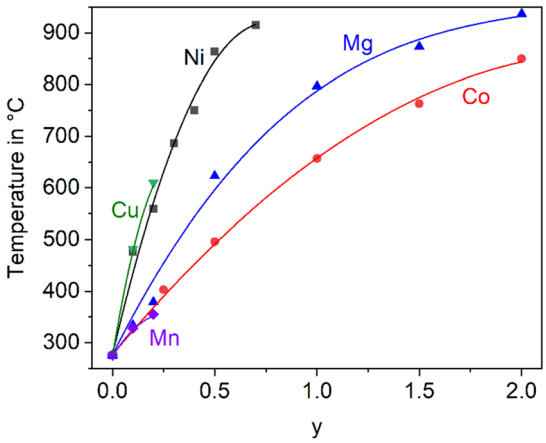

Fig. 5 Temperature of the phase transition for solid solutions of $BaZn_{2-y}M_ySi_2O_7$ with M = Co, Cu, Mg, Mn, and Ni.[2,5,22,23] The lines are drawn as a guide for the eyes.

lengths of *a*- and *c*-axes increase as expected, the *b*-axis contracts, *i.e.*, the CTE in the direction of the *b*-axis is negative.

3. Solid solutions based on $BaZn_2Si_2O_7$

3.1 Substitution of Zn^{2+} by divalent metal cations

In the literature, the total replacements of Zn^{2+} by Mg^{2+} or Co^{2+} and also, a partial replacement of Zn^{2+} by Ni^{2+} were reported.[2,5,22] In any case, a substitution of Zn^{2+} results in a shift of the phase transition to higher temperature. The thermal expansions of the end members of the solid solution series containing Zn^{2+}, Co^{2+} and Mg^{2+} are displayed in Fig. 4. In the case of the dilatometry results presented in Fig. 4, the phase transition changes the microstructure of the specimens considerably and the data allow only a purely qualitative consideration. Especially in the case of $BaZn_2Si_2O_7$, very different dilatometric curves can be found in the literature (see ref. 2 and 5), which is due to the formation of cracks during phase transition. $BaZn_{2-y}M_ySi_2O_7$ solid solutions show qualitatively the same behaviour, however, the phase transition is continuously shifted to higher temperatures with decreasing Zn^{2+} concentration as shown in Fig. 5. Simultaneously, the volume effect, which runs parallel to the phase transition decreases and is by far not as high as for $BaZn_2Si_2O_7$.

Mg^{2+} and Co^{2+} may totally replace Zn^{2+} without changing the crystal structure, while in the case of Cu^{2+} and Ni^{2+}, a 100% substitution is not possible. In the literature, an end member $BaCu_2Si_2O_7$ is reported, however, the crystal structure is different from the $BaZn_2Si_2O_7$ phases.[24] A complete substitution of Zn^{2+} by Mn^{2+} is also reported in ref. 25, however, phase transition temperatures above room temperature are only given for a lower degree of substitution (compare Fig. 5).

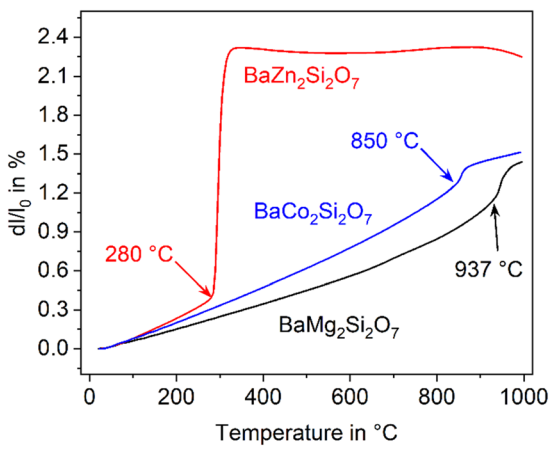

Fig. 4 Comparison of the dilatometric thermal expansion of $BaZn_2Si_2O_7$, $BaCo_2Si_2O_7$, and $BaMg_2Si_2O_7$.

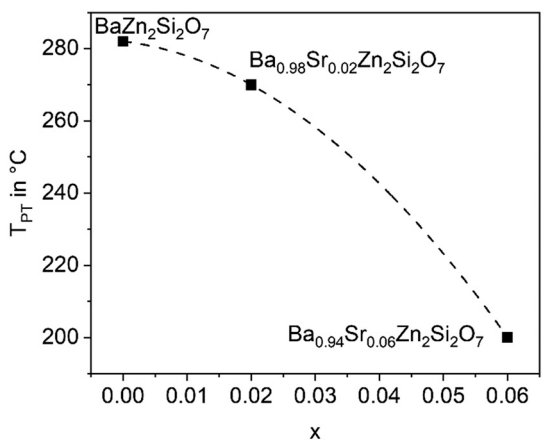

Fig. 6 Phase transition temperature (dilatometry) as a function of *x* in $Ba_{1-x}Sr_xZn_2Si_2O_7$ solid solutions.

3.2 Substitution of Ba^{2+} by Sr^{2+}

The substitution of Ba^{2+} by Sr^{2+} has the opposite effect as the Zn^{2+} replacement. If only 5% of Ba^{2+} are replaced by Sr^{2+}, the phase transition temperature decreases notably. This is shown in Fig. 6 for different replacements of Ba^{2+} against Sr^{2+}. Already if 10% of Ba^{2+} are replaced by Sr^{2+}, the phase transition temperature cannot be observed above room temperature. It is not exactly known whether the phase transitions occur at temperatures below room temperature, however, if 20% Ba^{2+} are substituted against Sr^{2+}, the high temperature phase is still stable at 100 K.[26]

Fig. 7 presents the thermal expansion of $Ba_{1-x}Sr_xZn_2Si_2O_7$ samples for various x-values. The CTEs are small up to a temperature of 400 °C and then increase. A smaller degree of substitution is favourable to achieve a negative CTE. Fig. 8 shows the lattice parameters of the $Ba_{0.6}Sr_{0.4}Zn_2Si_2O_7$ solid solution as a function of the temperature. It is shown that the a-axis as well as the c-axis expand during heating, while the b-axis strongly contracts. The volume of the unit cell decreases up to a temperature of 400 °C and then increases again.

To study the origin of the negative CTE, single crystal X-ray diffraction was performed at temperatures of 220, 293 and 353 K. Fig. 9 shows a part of the network formed by ZnO_4 (red) and SiO_4 tetrahedra (yellow). The crystallographic c-axis is perpendicular to the drawing plane, while the b-axis is arranged vertically. With increasing temperature, two bridged ZnO_4 tetrahedra rotate in opposite directions. Simultaneously, the ZnO_4- and SiO_4-units, deform. This leads to a shortening of the crystallographic b-axis.[27] These experimental observations were confirmed by simulations using density functional theory.[27]

The phase transition temperatures as a function of the chemical compositions were calculated by density functional theory simulations.[28] In Table 1, the calculated phase transition temperatures as well as those determined by dilatometry or DSC are summarized. The differences in the phase transition temperatures can be explained by the higher inaccuracy of simulated phase transition temperatures.

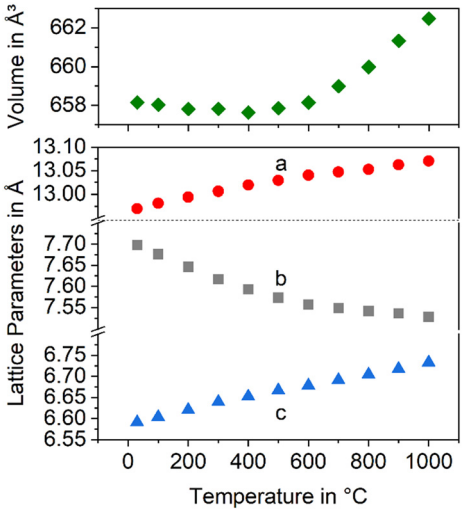

Fig. 8 Lattice constants and unit cell volume of the $Ba_{0.6}Sr_{0.4}Zn_2Si_2O_7$ solid solutions as a function of temperature.

3.3 Substitution of Ba^{2+} by Sr^{2+} and Zn^{2+} by other divalent cations

In analogy to the replacement of Zn^{2+} in the $BaZn_2Si_2O_7$ lattice, also in the $Ba_{1-x}Sr_xZn_2Si_2O_7$ lattice, Zn^{2+} can be substituted by other divalent cations. Generally, Zn^{2+} (ionic radius from ref. 29: 74 pm) can be substituted in the $Ba_{1-x}Sr_xZn_2Si_2O_7$ lattice by cations with similar ionic radii. The latter should be in the range from 80 pm (Mn^{2+}) to 92 pm (Co^{2+}).

In Table 2, the mean CTEs from HT-XRD of different compositions are summarized. The pure Zn-compound has a CTE of 0.7×10^{-6} K^{-1}. This value decreases when Zn^{2+} is substituted. A higher degree of substitution with one and the same element leads to smaller CTEs. If the degree of

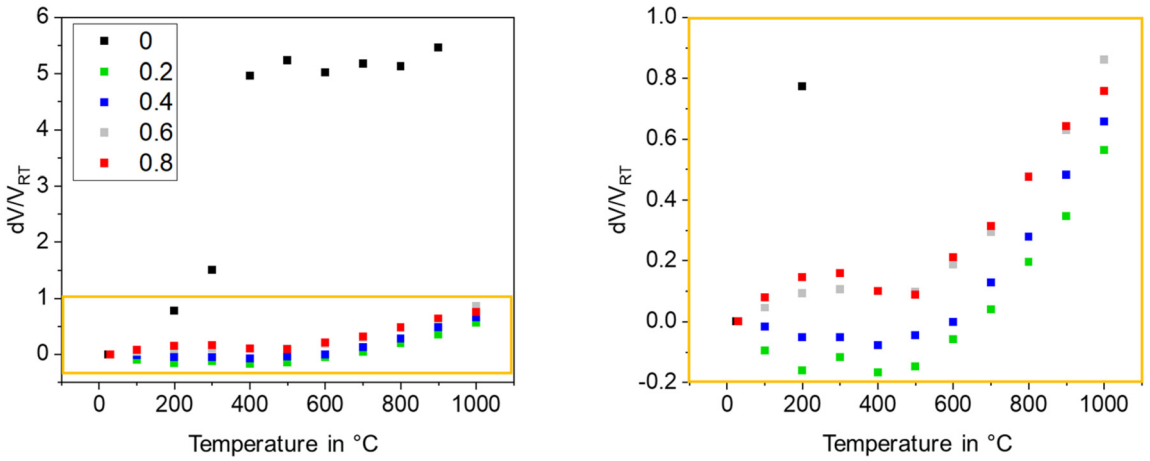

Fig. 7 Thermal expansion of $Ba_{1-x}Sr_xZn_2Si_2O_7$ as a function of the temperature for various x-values.

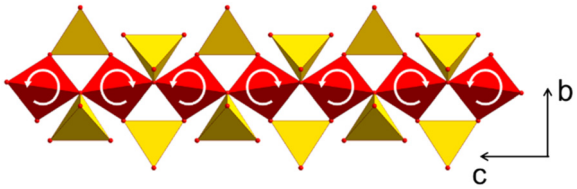

Fig. 9 Part of the network formed by ZnO_4 (red) and SiO_4 tetrahedra (yellow). With increasing temperature, ZnO_4 tetrahedra rotate, which results in a stretching of the ZnO_4-chain in the direction of the *c*-axis and a shortening in the *b*-direction. Redrawn from ref. 9.

substitution is kept constant, the lowest CTE is observed if Zn^{2+} is substituted by ions, which strongly shift the phase transition temperature. In Fig. 5, the effect of substitution on the phase transition temperature is shown. Ni^{2+} and Cu^{2+} have a larger effect than equimolar concentrations of the other ions and their incorporations lead to smallest CTEs. The CTE is lowest, if the degree of substitution is slightly below the limit which leads to the formation of the LT-phase with high thermal expansion.

3.4 Substitution of Si^{4+} by Ge^{4+}

In a $BaZn_2Si_2O_7$ lattice, up to 75% Si^{4+} can be replaced by Ge^{4+} without changing the phase while larger Ge^{4+}-concentrations lead to the formation of secondary phases, such as Zn_2GeO_4.[30,31] As shown in Fig. 10, the temperature of the phase transition increases linearly with increasing Ge concentration from 280 °C for $BaZn_2Si_2O_7$ to around 700 °C for $BaZn_2Si_{0.5}Ge_{1.5}O_7$ an hence, in analogy to the substitution of Zn^{2+} by other divalent cations, the monoclinic low temperature phase is increasingly stabilized.

In a $Ba_{1-x}Sr_xZn_2Si_2O_7$ solid solution, equimolar replacement of 50% of Si^{4+} by Ge^{4+}, still results in the formation of the orthorhombic high temperature phase. As shown in Fig. 11, the unit cell parameters increase linearly with the degree of substitution.

Fig. 12 shows lattice parameters of the orthorhombic high temperature phase with the composition $Ba_{0.5}Sr_{0.5}Zn_2SiGeO_7$. In analogy to $Ba_{0.5}Sr_{0.5}Zn_2Si_2O_7$, the *a*- and the *c*-axis expand during heating while the *b*-axis contracts. The volume of the unit cell decreases up to a temperature of 400 °C and then increases.

Table 2 Mean CTEs for the temperature range from 30 to 300 °C for $Ba_{0.5}Sr_{0.5}Zn_{1.9}M_{0.1}Si_2O_7$ with different elements M (data taken from ref. 23)

Element M	$CTE_{30-300°C}$ in $[10^{-6}\ K^{-1}]$
Mg	0.5
Co	0.1
Mn	−0.3
Ni	−1.6
Cu	−2.0

3.5 Thermal expansion and its anisotropy of solid solutions based on $Ba_{1-x}Sr_xZn_2Si_2O_7$

As shown above, the thermal expansion of solid solutions based on $BaZn_2Si_2O_7$ strongly depends on the substitution of Ba^{2+} by Sr^{2+}, of Zn^{2+} by other bivalent elements and of Si^{4+} by Ge^{4+}. Another important issue, however, is the degree of anisotropy of the thermal expansion. Generally, in all $Ba_{1-x}Sr_xZn_2Si_2O_7$ solid solutions, the CTE of the crystallographic *b*-axis is strongly negative, while those of the *a*- and *c*-axes are positive. In the following, as a measure of the anisotropy, the difference of the CTEs of the axis with the highest and the smallest were taken (see Fig. 13). The data were all extracted from high temperature XRD. The "anisotropy" values were all in the range from 42 to 81 × 10^{-6} K^{-1}.

There is a general trend that samples with higher CTE possess a smaller anisotropy. For example, for the series $Ba_{1-x}Sr_xZn_2Si_2O_7$ (without substitution of the Zn^{2+} position) the anisotropy decreases continuously from x = 0.2 to x = 0.8 (see black squares).

All other data are attributed to samples with the composition $Ba_{0.5}Sr_{0.5}Zn_{2-y}M_ySi_{2-z}Ge_zO_7$. For a particular cation M^{2+} substituting y = 0.1 Zn^{2+}, the CTE gets more negative, however, the anisotropy increases. This effect is most pronounced for Cu^{2+}, followed by Ni^{2+}, and Mn^{2+}. Also, in the case of Co^{2+} and Mg^{2+}, the effect is observed. Substitution of Si^{4+} by Ge^{4+} has a similar effect. Increasing *y*-values (*i.e.* increasing substitutions of Zn) lead to further increasing anisotropies and to further more negative CTEs in most cases. In summary, the maximum concentration of divalent cations substituting Zn^{2+}, where still the high temperature phase occurs leads to the most negative CTEs,

Table 1 Experimentally determined and calculated phase transition temperatures of various phases in the system $Ba_{1-x}Sr_xZn_{2-2y}Mg_{2y}Si_2O_7$ (values taken from ref. 2 and 28)

Chemical composition (mol%)	T_t experimental (°C)	T_t calculated (°C)
$BaZn_2Si_2O_7$	277[a]	222[c]
$BaZn_{1.5}Mg_{0.5}Si_2O_7$	623[a]	567[c]
$BaZnMgSi_2O_7$	797[a]	775[c]
$BaZn_{0.5}Mg_{1.5}Si_2O_7$	873[a]	980[c]
$BaMg_2Si_2O_7$	937[a]	869[c]
$Ba_{0.5}Sr_{0.5}ZnMgSi_2O_7$	392[a]	274[c]
$Ba_{0.75}Sr_{0.25}Zn_{0.5}Mg_{1.5}Si_2O_7$	588[b]	548[c]

[a] Determined by DSC. [b] Determined by dilatometry. [c] Calculated values.

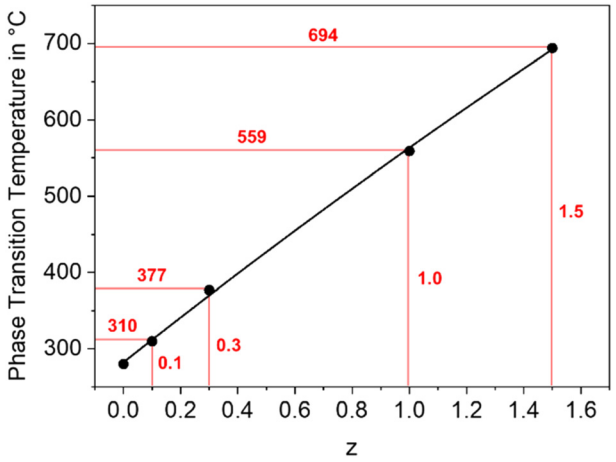

Fig. 10 Phase transition temperature of $BaZn_2Si_{2-z}Ge_zO_7$ solid solutions as a function of the Ge concentration.

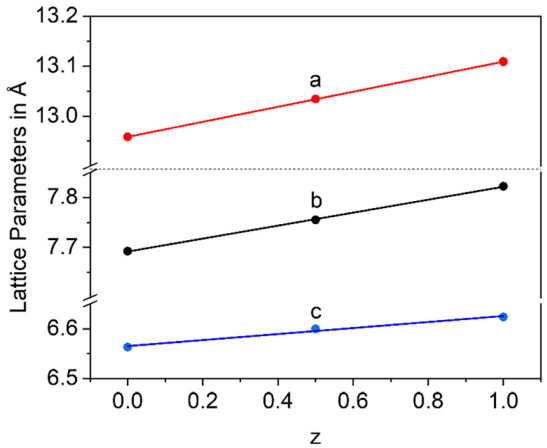

Fig. 11 Lattice parameters of $Ba_{0.5}Sr_{0.5}Zn_2Si_{2-z}Ge_zO_7$ solid solutions with z = 0, 0.5 and 1.

whereas a larger degree of substitution results in a decrease of the anisotropy.

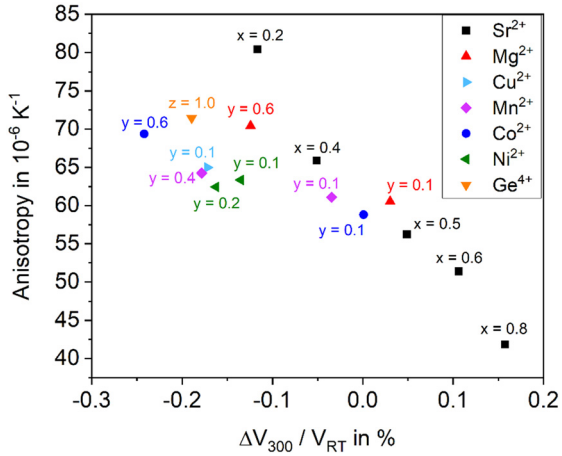

Fig. 13 Anisotropy *versus* the mean change of the volume of $Ba_{1-x}Sr_xZn_{2-y}M_ySi_{2-z}Ge_zO_7$ samples. If the Sr^{2+} concentration varies on the expense of Ba^{2+}, Zn^{2+} is not substituted (y = 0, *i.e.*, sample series $Ba_{1-x}Sr_xZn_2Si_2O_7$). If Zn^{2+} or Si^{4+} are replaced, the x-value is kept constant with x = 0.5 (sample series $Ba_{0.5}Sr_{0.5}Zn_{2-y}M_ySi_{2-z}Ge_zO_7$).

4. Glass formation in the BaO/ZnO/SiO_2 and BaO/SrO/ZnO/SiO_2 systems

The stoichiometric compounds $Ba_{1-x}Sr_xZn_2Si_2O_7$ and $BaZn_2Si_2O_7$ do not form glasses. That is due to the lack of a network structure. Assuming BaO and ZnO occur as network modifier, a continuous network is not formed and the mean network connectivity is equal to 1. That means, an $Si_2O_7^{6-}$ structure should be predominant which charges are compensated in the average by one Ba^{2+} and two Zn^{2+} ions. This simple consideration fully explains that stoichiometric melts crystallize during cooling. The glass formation ranges of the systems BaO–ZnO–SiO_2 and SrO–ZnO–SiO_2 are given in ref. 32–34. To overcome the problem of spontaneous crystallization, the concentration of network formers has to be increased.

In the case of the system BaO/ZnO/SiO_2 from which mainly materials with high CTEs should be crystallized, the

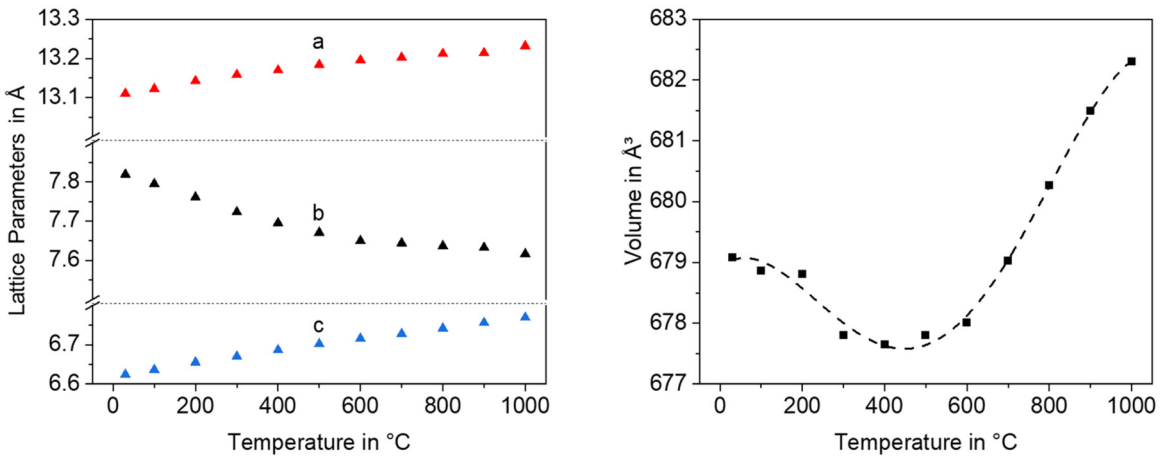

Fig. 12 Lattice parameters and unit cell volume of $Ba_{0.5}Sr_{0.5}Zn_2SiGeO_7$ as a function of temperature.

composition 18 BaO·27 ZnO·55 SiO_2 proved to be suitable for controlled precipitation of $BaZn_2Si_2O_7$. Here, the network connectivity is 2.36 which is just a little bit above the percolation threshold according to the percolation limit of 2.3.[35] At a lower network connectivity, the network is "floppy", *i.e.* no more rigid and nucleation is facilitated. Therefore, the crystallization tendency should be comparatively low in comparison to a glass with the stoichiometry 20 BaO·40 ZnO·40 SiO_2. In the 18 BaO·27 ZnO·55 SiO_2 composition, the Ba/Zn ratio was chosen larger than 0.5 because an excess of barium should result in the additional crystallization of barium silicates, which also have high CTEs in the range from 12 to 15 × 10^{-6} K^{-1}, but the crystallization of Zn_2SiO_4 (willemite) with its exceptionally small CTE should be avoided.[36–38]

In the system SrO–ZnO–SiO_2, a compound with very high thermal expansion does not precipitate. In a glass with the mol% composition 16 SrO·35 ZnO·45 SiO_2·1 ZrO_2·1 La_2O_3·2 B_2O_3, $Sr_2ZnSi_2O_7$ and Zn_2SiO_4 as major crystalline phases are described.[39] The crystallized glass has a CTE of around 7 × 10^{-6} K^{-1}. Higher SrO-concentrations may additionally lead to the precipitation of $SrSiO_3$.[40,41] The system BaO/SrO/ZnO/SiO_2 has a lower tendency towards crystallization than the system BaO/ZnO/SiO_2. This should be due to the occurrence of three different network modifying components which decreases the tendency towards crystallization. The glass with the composition 8 BaO·8 SrO·34 ZnO·50 SiO_2 can be obtained by melt quenching. It does not form a real network structure, however, the network connectivity (assuming again BaO and ZnO acting as network modifiers) is equal to two and hence something like a chain structure or a combined ring and chain structure should be formed. Another, more complex glass composition in this system is 8 BaO·8 SrO·35 ZnO·45 SiO_2·1 ZrO_2·1 La_2O_3·2 B_2O_3. Here, the concentration of ZnO was increased by 3 mol% (in comparison to that of the alkaline earths) to avoid the crystallization of high CTE barium silicates. Furthermore, the tendency towards crystallization was decreased by the addition of SiO_2, B_2O_3, ZrO_2 and La_2O_3. Minor concentrations of the latter two are well known nucleation inhibitors in melts of high basicity.[42,43] It should be noted, however, that higher concentrations of ZrO_2 have a nucleating effect in many systems.[44]

If glasses containing both BaO and SrO together with ZnO and SiO_2 are crystallized, the stability range of the HT-phase is much smaller than of ceramics obtained *via* mixed oxide routes.[39,45] While in the case of ceramics, the HT-phase is stable for $0.2 < x < 0.8$, in a glass with the same BaO/SrO ratio, both the LT- and the HT-phases are formed. The sole crystallization of the HT phase from glasses is observed for $0.5 < x < 0.8$.[39] Higher SrO concentrations lead to the formation of $Sr_2ZnSi_2O_7$ and Zn_2SiO_4. The different phase formation of compact samples in comparison to powdered samples is supposedly due to the anisotropy of the thermal expansion which leads to notable internal stresses during cooling.

The phase transitions, observed in crystalline $BaZn_2Si_2O_7$ and isostructural compounds, can also be found in the respective crystallized glasses. In solid solutions precipitated from glasses, the phase transitions are shifted to higher values. In a glass with the molar composition 19 ZnO·27 BaO·54 SiO_2, from which $BaZn_2Si_2O_7$ was precipitated, the phase transition temperature occurs at 380 °C, *i.e.* around 100 K higher than in the stoichiometric crystalline phase.[46] Furthermore, the jump in volume is not observed; instead, a kink is visible.

5. Crystallization behaviour of glasses

Glasses in the system BaO/ZnO/SiO_2 show surface crystallization. Compounds, such as SrO, MgO, MnO, CoO, NiO, CuO, or GeO_2 used to crystallize solid solutions do not promote bulk nucleation. Nevertheless, the addition of nucleation agents, noble metals or oxidic compounds may lead to bulk nucleation. The latter are oxides of metals with high valency mostly in the range of four to six, such as TiO_2, ZrO_2 or a mixture hereof.[44,47–49]

5.1 Surface crystallization

When thermally treated at temperatures not too far above T_g, glasses in the BaO/ZnO/SiO_2 and BaO/SrO/ZnO/SiO_2 systems show surface crystallization. In the BaO/SrO/ZnO/SiO_2 system, nucleation at the surface already leads to an orientation of the *a*- or *b*-axis parallel to the surface.[50] The highest growth velocity, however, is along the crystallographic *c*-axis (see Fig. 14). The crystals grow for some microns along the surface and then the growth direction changes continuously until the *c*-axis grows towards the bulk.[51] A possible explanation might be oriented nucleation. However, this

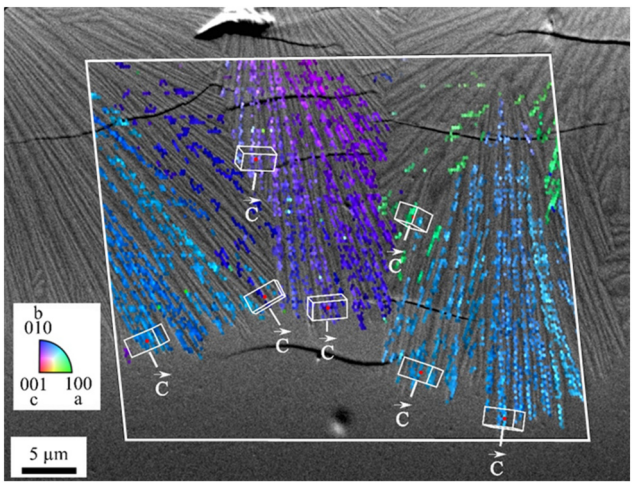

Fig. 14 Orientation of surface crystals with growing direction from the top to the bottom. The micrograph shows a cross section after crystallization for 1.5 h at 790 °C. The colour coded part of the micrograph is a superposition with an inverse pole figure map of an EBSD scan. (redrawn from ref. 50).

effect, which is described in a recent review, was not proven in detail for the glasses described here.[52] The change in the growth direction is denoted as "crystal selection" or "survival of the fastest" and is due to the fact that crystals hinder each other during crystal growth and only crystals which are oriented with their fastest growing axis approximately perpendicular to the surface may survive.

In the SEM micrograph (Fig. 14), a surface crystallized sample with the composition 8 BaO·8 SrO·34 ZnO·50 SiO_2 thermally treated 790 °C for 1.5 h is presented. The micrograph shows some cracks perpendicular to the long axis, the *c*-axis of the respective crystals which are supposedly formed during cooling of the sample. The thicknesses of the layers increase linearly with time (within the accuracy of the measurement). Hence, compounds which are not incorporated in the crystal, *i.e.* some excess SiO_2 are not increasingly enriched at the growth front and do not form a diffusion barrier which decelerates crystal growth with time.[53]

5.2 Bulk nucleation, effect of nucleation agents

5.2.1 Metallic nucleation agents. Using metallic nucleation agents, solutions of noble metals salts such as $PtCl_4$, $AuCl_3$ and $AgNO_3$ are given to the raw materials from which the glass is to be melted. The concentrations necessary to achieve nucleation are 50 to 200 ppm for platinum compounds,[54–56] 0.01 to 0.1 mol% for gold,[57,58] and at least 0.1 mol% for silver.[59,60] At high temperatures, the respective noble metal compounds are homogeneously dissolved as Pt^{2+}, Au^{+} or Ag^{+}. During subsequent cooling, these ions react with redox agents which have intentionally been added to the batch. The most commonly added component is antimony, however, also arsenic or tin can be used. At high temperatures, these compounds mainly occur as Sb^{3+}, As^{3+} or Sn^{2+}. During cooling a redox reaction of the following type (for the example antimony) takes place:

$$2Ag^{+} + Sb^{3+} \rightarrow 2Ag + Sb^{5+} \quad (1)$$

These redox reactions can be enhanced by a thermal treatment step at temperatures slightly above the glass transition temperature. The metals form clusters with sizes in the range from 5 to some hundred nanometres or even a few microns, which act as nucleation centres for a subsequent crystallization.

In principle, bulk nucleation can be achieved by the addition of platinum as well as of silver. In the case of silver, the $Ba_{0.5}Sr_{0.5}Zn_2Si_2O_7$ crystals do not directly grow on the silver nano crystals but an intermediate phase is formed, which seems to be an antimony doped willemite type (Zn_2SiO_4) phase.[61] Only the formation of this core shell structure (see Fig. 15) initiates $Ba_{0.5}Sr_{0.5}Zn_2Si_2O_7$ crystallization. Fig. 16 shows micrographs of BaO/SrO/ZnO/SiO_2 based glass ceramics with different Ag_2O and Sb_2O_3 concentrations, crystallized under the same conditions (nucleation: 675 °C for 20 h, crystal growth; 760 °C for 5 h). Both samples show as main crystalline phase $Ba_{0.5}Sr_{0.5}Zn_2Si_2O_7$ as well as metallic silver (see small bright spots). The sample with Ag and Sb_2O_3 concentrations of 0.3 and 1.5 mol%, respectively shows a fairly coarse microstructure and numerous cracks. By contrast, the sample with 0.6 mol% Ag and 3 mol% Sb_2O_3 possesses a much finer microstructure. That is due to the occurrence of much more Ag particles. The twice as high silver concentration but also the higher Sb^{3+} concentration led to a much more effective nucleation and much smaller $Ba_{0.5}Sr_{0.5}Zn_2Si_2O_7$ crystals.

5.2.2 Oxidic nucleation agents. As oxidic nucleation agents, comparatively high ZrO_2 concentrations of ≥6 mol% can be used.[62,63] Additionally, P_2O_5,[64] both P_2O_5 and Ce_2O_3,[65] WO_3 (ref. 66) and Ta_2O_5 (ref. 67) were reported to act as nucleation agents. It should be noted that the oxidic nucleation agents up to now reported in the literature for these glass systems are by far not as effective as the noble metals.

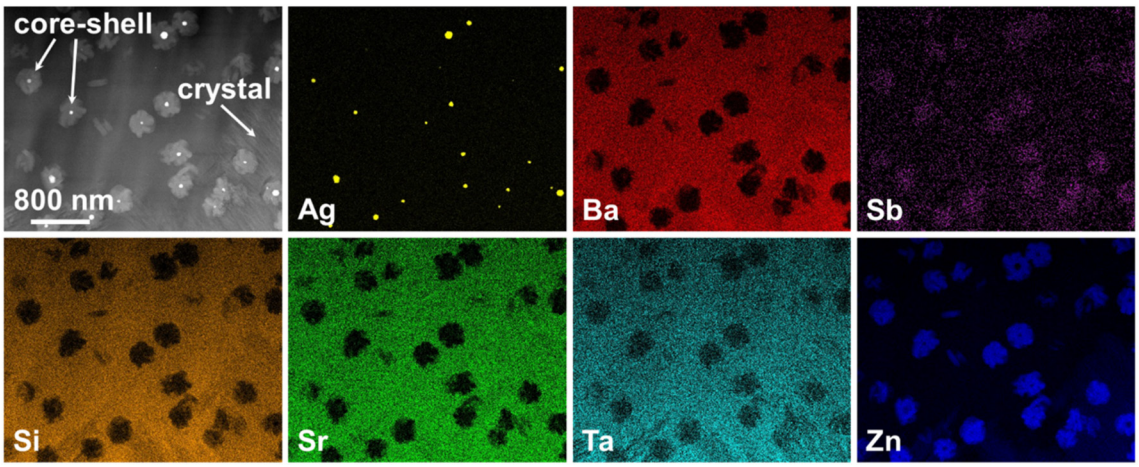

Fig. 15 STEM micrograph and elemental distribution of core–shell structures within a glass with the molar composition 9.5 BaO·9.5 SrO·38 ZnO·38 SiO_2·3.2 Ta_2O_5·1.5 Sb_2O_3·0.3 Ag after a two-step heat treatment at 675 °C for 10 h and 760 °C for 5 h and related EDX maps. The main crystal phase (denoted as "crystal") is composed of $Ba_{0.5}Sr_{0.5}Zn_2Si_2O_7$.

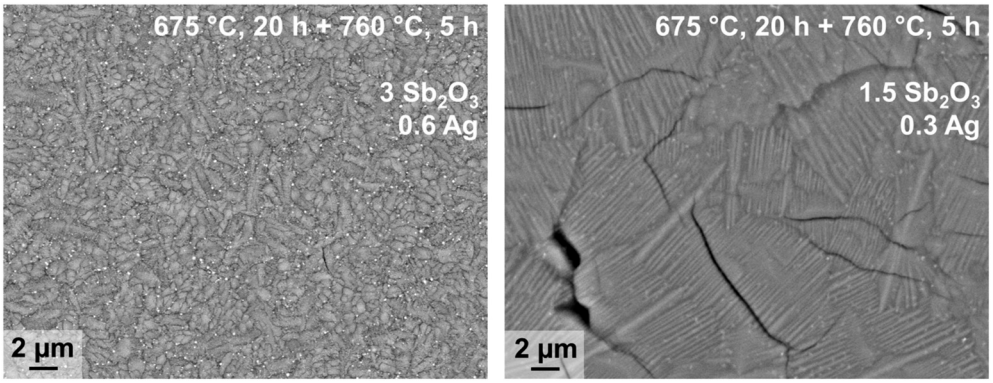

Fig. 16 SEM micrographs of glasses from the system BaO–SrO–ZnO–SiO_2 nucleated with Ag + Sb_2O_3 in different concentrations after a two-step thermal treatment. Both micrographs show the same magnification.

Fig. 17 shows the microstructure of a glass–ceramic with the composition 7.5 BaO·7.5 SrO·34 ZnO·43 SiO_2·7 ZrO_2·1 TiO_2 crystallized at 750 °C for 48 h and at 840 °C for 30 min.[63] Large crystals within the glass volume can be found, which seem to start growing from only one nucleus. Furthermore, crystal agglomerates of the $Ba_{0.5}Sr_{0.5}Zn_2Si_2O_7$ phase with diameters in the range from 40 to 60 µm are observed. The agglomerates consist of bundles of various crystals which all have similar orientations (see for example the crystal in the upper right corner of Fig. 17). The agglomerates are composed by 6 to 10 bundles with different orientations. The long dimension of the crystals is the crystallographic *c*-axis, as evidenced by electron backscatter diffraction. The nuclei themselves which possibly consist of ZrO_2 could not be detected.

Fig. 18 shows an SEM micrograph of a sample with the composition 9.4 BaO·9.4 SrO·37.6 ZnO·37.6 SiO_2·4 P_2O_5·2 Ce_2O_3 which is equal to 18.8 ($Ba_{0.5}Sr_{0.5}Zn_2Si_2O_7$)·4 P_2O_5·2 Ce_2O_3.[65] The addition of P_2O_5 and Ce_2O_3 to the stoichiometric compound obviously extends the glass forming range notably. During thermal treatment at 690 °C for 20 h and subsequently at 850 °C for 1 h, first surface crystallization of $Ba_{0.5}Sr_{0.5}Zn_2Si_2O_7$, Zn_2SiO_4, and CeO_2 can be observed. Furthermore, the crystallization of $(Ba,Sr)_5(PO_4)_3Cl$, a phase with the hexagonal apatite ($Ca_5P_3O_{12}OH$) structure (space group $P6_3/m$), occurred (see the bright crystals with hexagonal shape in Fig. 18). The *c*-axes of these crystals are oriented approximately perpendicular to the cut plane. The crystals growing around them are $Ba_{0.5}Sr_{0.5}Zn_2Si_2O_7$ which is also oriented with the *c*-axis in the same manner and hence epitaxial growth on the apatite crystal is assumed.

6. Sintering of glass powders and sol–gel derived glasses

6.1 Sinter crystallization of glasses

If glasses are powdered, pressed into shape and subsequently sintered, the preparation procedure is denoted as "sinter crystallization". It is assumed that first sintering due to viscous flow occurs and subsequently, nucleation at the inner surface of the sintering specimen. During the continuous heat treatment, complete densification takes place until all pores are eliminated and subsequently crystal growth occurs. The size of the crystals is usually in the same range as that of the powder particles. By contrast to the crystallization of bulk glasses, sinter crystallization leads to a homogeneous

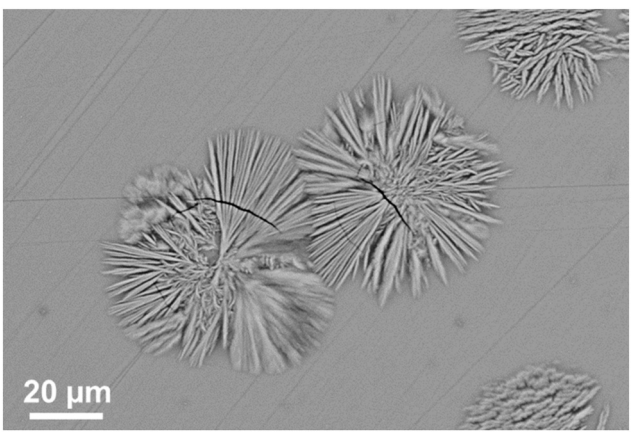

Fig. 17 Microstructure of a sample with the composition 7.5 BaO·7.5 SrO·34 ZnO·43 SiO_2·7 ZrO_2·1 TiO_2 crystallized at 750 °C for 48 h and at 840 °C for 30 min.

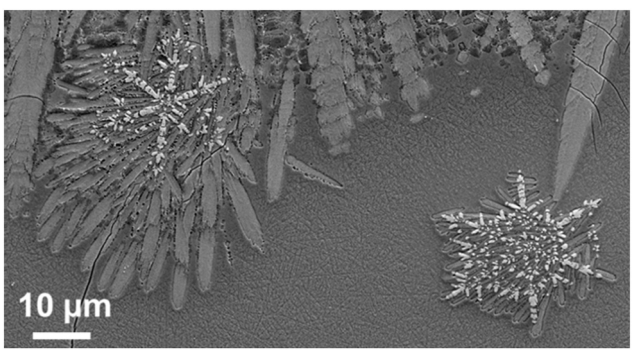

Fig. 18 SEM micrograph with the composition 9.4 BaO·9.4 SrO·37.6 ZnO·37.6 SiO_2·4 P_2O_5·2 Ce_2O_3, crystallized at 690 °C for 20 h and subsequently at 850 °C for 1 h.

microstructure also if the corresponding bulk glass shows solely surface crystallization. Sinter crystallization of glasses in the system $BaO/ZnO/SiO_2$ is mostly applied to sealing applications and results in specimens with CTEs in the range from 10–15 × 10^{-6} K^{-1}. By contrast, sinter crystallized glass ceramics in the system $BaO/SrO/ZnO/SiO_2$ has its greatest potential in the preparation of materials with zero or negative CTE. Fig. 19 shows a microstructure of a sample with the composition 8 BaO·8 SrO·35 ZnO·45 SiO_2·1 ZrO_2·1 La_2O_3·2 B_2O_3 sinter crystallized at 800 °C for 1 h using a grain size <63 μm.[45] The dark areas in between the crystals mark the residual glassy phase, enriched in SiO_2 with a lower mean atomic number than the crystal phase. Although no EDX mapping is shown in Fig. 19, it has been confirmed experimentally on similar glass compositions by EDX that the dark phase is enriched in SiO_2.[68]

The thermal expansion is strongly affected by the grain size of the used glass powder. In general, the CTE is more negative, if the used grain size is larger. In Fig. 20, this effect is shown for sinter crystallized glass ceramics all prepared by thermal treatment at 950 °C for 1 h. The most negative CTE is obtained using the grain size fraction from 100 to 200 μm, while using the grain size fraction from 63 to 100 μm results in a material of positive CTE. Surprisingly, the CTE of some prepared materials determined by dilatometry is much more negative than that determined by high temperature XRD. This effect is due to the strong thermal expansion of the crystallographic *b*-axis and the contraction of the crystallographic *a*- and *c*-axis during cooling. This strongly anisotropic thermal expansion leads to stresses formed during cooling which result in microcracks. During heating, the microcracks will successively be closed while they are opened again during cooling.

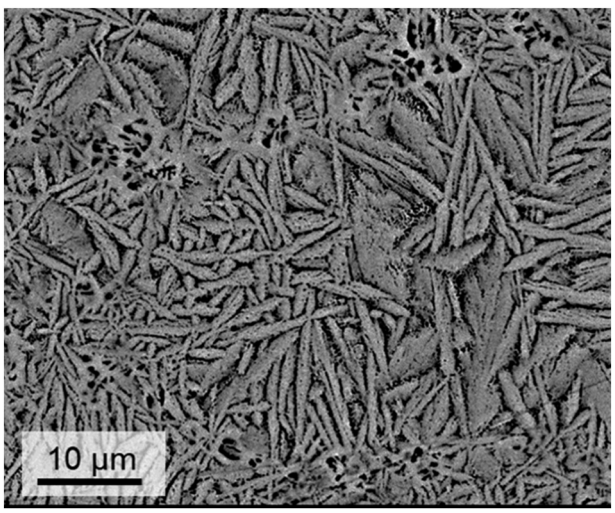

Fig. 19 Microstructure of a sinter crystallized sample with the composition 8 BaO·8 SrO·35 ZnO·45 SiO_2·1 ZrO_2·1 La_2O_3·2 B_2O_3 sintered at 800 °C for 1 h. Redrawn from ref. 45.

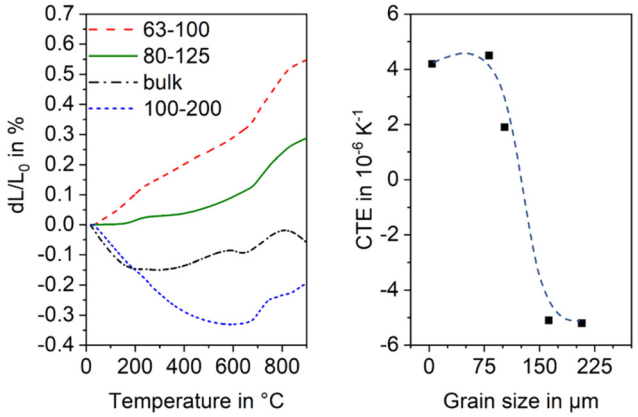

Fig. 20 Thermal expansion of sinter crystallized glass powders with the composition 8 BaO·8 SrO·35 ZnO·45 SiO_2·1 ZrO_2·1 La_2O_3·2 B_2O_3 sintered at 950 °C for 1 h. Left: Dilatometric measurements. Right: CTE *vs.* grain size of sintered powders. The dashed line is just a guide for the eyes. Redrawn from ref. 45.

6.2 Sintering of sol–gel powders

Sol–gel derived powders generally possess small crystallites with sizes in the few to some 10 nm range which hence show high sinter activity.[69,70] In order to obtain $Ba_{1-x}Sr_xZn_2Si_2O_7$, sol–gel powders were prepared as previously described.[10] After hydrolysis, polycondensation and drying, the gel was milled and subsequently thermally treated at 530 °C. Then the calcined powder was hot pressed at 1100 °C for 10 min using a uniaxial pressure of 40 MPa which resulted in almost full densification. Dilatometry showed negative thermal expansion up to a temperature of 80 °C. At higher temperatures, the CTE increases steadily. Hence, the range of negative thermal expansion is shifted to lower temperatures than in the case of a stoichiometric crystalline compound. In analogy, a $BaZn_2Si_2O_7$ sample prepared *via* sol–gel route shows a lower phase transition temperature.

7. Remarks and outlook

The low temperature phase $BaZn_2Si_2O_7$ transfers to a high temperature phase at 280 °C which is accompanied by a volume increase of 3.3%. Substitution of Zn^{2+} against Mg^{2+}, Mn^{2+}, Ni^{2+}, Co^{2+} or Cu^{2+} or of Si^{4+} by Ge^{4+} results in solid solutions and in a shift of the phase transition to higher temperatures. If Ba^{2+} is partially replaced against Sr^{2+}, the phase transition temperature gets lower even below room temperature.

The most remarkable property of $BaZn_2Si_2O_7$ and solid solutions derived hereof are the CTEs. The low temperature phase has a high CTE in the range from 10 to 15 × 10^{-6} K^{-1}, which is approximately constant up to the phase transition temperature, for the case of a 100% replacement of Zn^{2+} against Co^{2+} up to 850 °C. The CTE of the high temperature phase is small or even negative. For a substitution of 10% Ba^{2+} against Sr^{2+}, a negative CTE is observed from room temperature up to a temperature of 500 °C.

The addition of network forming compounds to the stoichiometric $Ba_{1-x}Sr_xZnSi_2O_7$ and/or the addition of nucleation inhibitors enables the preparation of glasses by melt quenching. Controlled crystallization of such glasses results in surface nucleation. However, the addition of nucleating agents such as ZrO_2 or noble metals enables volume nucleation and the preparation of homogeneous glass ceramics. It should be mentioned that also the preparation of sintered ceramics from sol–gel derived powders with negative CTE is possible. Future developments should be focused on $Ba_{1-x}Sr_xZn_{2-y}M_ySi_{2-z}Ge_zO_7$ crystals with smaller crystallites, *i.e.*, a more effective homogeneous nucleation. Another important issue are glass ceramics containing $Ba_{1-x}Sr_xZn_{2-y}M_ySi_{2-z}Ge_zO_7$ crystals of less pronounced anisotropy in the thermal expansion.

Conflicts of interest

There are no conflicts to declare.

Acknowledgements

This work was funded by the German Federal Ministry of Education and Research under the Grant Numbers 03VP01701 and 03VP01702 and by the German Research Foundation (DFG) under Grant Number TH 2241/1-1.

References

1 J. H. Lin, G. X. Lu, J. Du, M. Z. Su, C.-K. Loong and J. W. Richardson Jr, *J. Phys. Chem. Solids*, 1999, **60**, 975–983.
2 M. Kerstan, M. Müller and C. Rüssel, *J. Solid State Chem.*, 2012, **188**, 84–91.
3 M. Kerstan, C. Thieme, A. Kobeisy and C. Rüssel, *J. Mater. Sci.*, 2017, **52**, 1789–1796.
4 D. Ehrt, A. Herrmann and M. Tiegel, *Phys. Chem. Glasses: Eur. J. Glass Sci. Technol., Part B*, 2011, **52**, 68–76.
5 M. Kerstan, C. Thieme, M. Grosch, M. Müller and C. Rüssel, *J. Solid State Chem.*, 2013, **207**, 55–60.
6 S. S. Mitra and S. K. Joshi, *J. Chem. Phys.*, 1961, **34**, 1462–1463.
7 F. Tietz, *Ionics*, 1999, **5**, 129–139.
8 M. K. Mahapatra and K. Lu, *Mater. Sci. Eng., R*, 2010, **67**, 65–85.
9 C. Thieme, H. Görls and C. Rüssel, *Sci. Rep.*, 2015, **5**, 18040.
10 M. Kracker, C. Thieme, J. Häßler and C. Rüssel, *J. Eur. Ceram. Soc.*, 2016, **36**, 2097–2107.
11 B. Li, S. Wang and Y. Fang, *J. Alloys Compd.*, 2017, **693**, 9–15.
12 J. Liu, Q. Wang, Z. Zhang, Q. Zeng, H. Peng and Q. Chang, *J. Non-Cryst. Solids*, 2022, **576**, 121226.
13 H. Bach and D. Krause, *Low Thermal Expansion Glass Ceramics*, Springer, Berlin, Heidelberg, 2nd edn, 2005.
14 G. D. Barrera, J. A. O. Bruno, T. H. K. Barron and N. L. Allan, *J. Phys.: Condens. Matter*, 2005, **17**, R217–R252.
15 E. D. Zanotto, *Am. Ceram. Soc. Bull.*, 2010, **89**, 19–27.
16 R. M. Hovhannisyan, *Glass Technol.*, 2003, **44**, 96–100.
17 J. F. MacDowell, *J. Am. Ceram. Soc.*, 1990, **73**, 2287–2292.
18 D. Tauch and C. Rüssel, *J. Non-Cryst. Solids*, 2005, **351**, 2294–2298.
19 T. A. Mary, J. S. O. Evans, T. Vogt and A. W. Sleight, *Science*, 1996, **272**, 90–92.
20 J. S. O. Evans, T. A. Mary, T. Vogt, M. A. Subramanian and A. W. Sleight, *Chem. Mater.*, 1996, **8**, 2809–2823.
21 R. D. Adams, R. Layland, C. Payen and T. Datta, *Inorg. Chem.*, 1996, **35**, 3492–3497.
22 C. Thieme and C. Rüssel, *J. Mater. Sci.*, 2015, **50**, 3416–3424.
23 C. Thieme, T. Waurischk, S. Heitmann and C. Rüssel, *Inorg. Chem.*, 2016, **55**, 4476–4484.
24 J. Janczak, R. Kubiak and T. Głowiak, *Acta Crystallogr., Sect. C: Cryst. Struct. Commun.*, 1990, **46**, 1383–1385.
25 J. Ma, C. D. Dela Cruz, T. Hong, W. Tian, A. A. Aczel, S. Chi, J.-Q. Yan, Z. L. Dun, H. D. Zhou and M. Matsuda, *Phys. Rev. B: Condens. Matter Mater. Phys.*, 2013, **88**, 144405.
26 C. Thieme and C. Rüssel, *Dalton Trans.*, 2016, **45**, 4888–4895.
27 A. Erlebach, C. Thieme, C. Müller, S. Hoffmann, T. Höche, C. Rüssel and M. Sierka, *Phys. Chem. Chem. Phys.*, 2020, **22**, 18518–18525.
28 A. Erlebach, G. Belhadj Hassine, C. Thieme, K. Thieme, C. Rüssel and M. Sierka, *Phys. Chem. Chem. Phys.*, 2021, **23**, 25533–25541.
29 R. D. Shannon, *Acta Crystallogr., Sect. A: Cryst. Phys., Diffr., Theor. Gen. Crystallogr.*, 1976, **32**, 751–767.
30 H. Koelmans and C. M. C. Verhagen, *J. Electrochem. Soc.*, 1959, **106**, 677–682.
31 C. Thieme and C. Rüssel, *Materials*, 2016, **9**, 631.
32 C. Lara, M. J. Pascual and A. Durán, *J. Non-Cryst. Solids*, 2004, **348**, 149–155.
33 M. Imaoka and T. Yamazaki, *Rep. Inst. Ind. Sci., Univ. Tokyo*, 1968, **8**, 241–273.
34 G. W. Cleek and C. L. Babcock, *NBS Monogr.*, 1973, **135**, 1–39.
35 I. Avramov, R. Keding and C. Rüssel, *J. Non-Cryst. Solids*, 2000, **272**, 147–153.
36 A. M. Hu, M. Li, D. L. M. Dali and K. M. Liang, *Thermochim. Acta*, 2005, **437**, 110–113.
37 M. Kerstan and C. Rüssel, *J. Power Sources*, 2011, **196**, 7578–7584.
38 M. Kerstan, M. Müller and C. Rüssel, *Mater. Res. Bull.*, 2011, **46**, 2456–2463.
39 C. Thieme, M. Schlesier, E. Oji Dike and C. Rüssel, *Sci. Rep.*, 2017, **7**, 3344.
40 B. Tiwari, A. Dixit and G. P. Kothiyal, *Int. J. Hydrogen Energy*, 2011, **36**, 15002–15008.
41 B. Tiwari, A. Dixit, C. G. S. Pillai, S. C. Gadkari and G. P. Kothiyal, *J. Am. Ceram. Soc.*, 2012, **95**, 1290–1296.
42 K. Thieme and C. Rüssel, *J. Eur. Ceram. Soc.*, 2014, **34**, 3969–3979.
43 K. Thieme and C. Rüssel, *J. Mater. Sci.*, 2015, **50**, 1488–1499.
44 M. Dittmer, C. F. Yamamoto, C. Bocker and C. Rüssel, *Solid State Sci.*, 2011, **13**, 2146–2153.
45 C. Thieme, M. Schlesier, C. Bocker, G. Buzatto de Souza and C. Rüssel, *ACS Appl. Mater. Interfaces*, 2016, **8**, 20212–20219.
46 C. Thieme and C. Rüssel, *Ceram. Int.*, 2015, **41**, 13310–13319.

47 E. Kleebusch, C. Patzig, M. Krause, Y. Hu, T. Höche and C. Rüssel, *Sci. Rep.*, 2018, **8**, 2929.
48 T. Höche, M. Mäder, S. Bhattacharyya, G. S. Henderson, T. Gemming, R. Wurth, C. Rüssel and I. Avramov, *CrystEngComm*, 2011, **13**, 2550–2556.
49 C. Patzig, T. Höche, M. Dittmer and C. Rüssel, *Cryst. Growth Des.*, 2012, **12**, 2059–2067.
50 M. Kracker, L. Vladislavova, C. Thieme, T. Zscheckel, K. Thieme, T. Höche and C. Rüssel, *RSC Adv.*, 2017, **7**, 44834–44842.
51 M. Kracker, T. Zscheckel, C. Thieme, K. Thieme, T. Höche and C. Rüssel, *CrystEngComm*, 2019, **21**, 1320–1328.
52 W. Wisniewski and C. Rüssel, *Prog. Mater. Sci.*, 2021, **118**, 100758.
53 T. Waurischk, C. Thieme and C. Rüssel, *J. Mater. Sci.*, 2020, **55**, 10364–10374.
54 L. Vladislavova, C. Thieme, T. Zscheckel, C. Patzig, T. Höche and C. Rüssel, *J. Eur. Ceram. Soc.*, 2017, **37**, 4801–4808.
55 L. Vladislavova, C. Thieme, T. Zscheckel, T. Höche and C. Rüssel, *J. Alloys Compd.*, 2019, **793**, 705–714.
56 L. Vladislavova, M. Kracker, T. Zscheckel, C. Thieme and C. Rüssel, *J. Mater. Sci.*, 2018, **53**, 11204–11215.
57 M. Kracker, C. Thieme, K. Thieme, C. Patzig, L. Berthold, T. Höche and C. Rüssel, *RSC Adv.*, 2018, **8**, 6267–6277.
58 C. Thieme, M. Kracker, C. Patzig, K. Thieme, C. Rüssel and T. Höche, *J. Eur. Ceram. Soc.*, 2019, **39**, 554–562.
59 M. Kracker, C. Thieme, K. Thieme, T. Höche and C. Rüssel, *Ceram. Int.*, 2019, **45**, 18760–18766.
60 C. Thieme, K. Thieme, M. Kracker, C. Patzig, L. Berthold, T. Höche and C. Rüssel, *Ceram. Int.*, 2021, **47**, 1126–1132.
61 C. Thieme, L. Vladislavova, K. Thieme, C. Patzig, T. Höche and C. Rüssel, *J. Mater. Sci.*, 2022, **57**, 6607–6618.
62 L. Vladislavova, C. Thieme and C. Rüssel, *J. Mater. Sci.*, 2017, **52**, 4052–4060.
63 L. Vladislavova, M. Kracker, T. Zscheckel, C. Thieme and C. Rüssel, *Solid State Sci.*, 2018, **78**, 107–115.
64 K. Thieme, T. Zscheckel, C. Thieme, T. Höche and C. Rüssel, *J. Eur. Ceram. Soc.*, 2018, **38**, 2017–2026.
65 K. Thieme, T. Zscheckel, C. Thieme, M. Kracker, C. Rüssel and T. Höche, *Ceram. Int.*, 2018, **44**, 19970–19980.
66 C. Thieme, A. Erlebach, C. Patzig, K. Thieme, M. Sierka, T. Höche and C. Rüssel, *CrystEngComm*, 2018, **20**, 4565–4574.
67 S. Heitmann, K. Thieme, C. Thieme, M. Kracker, T. Höche and C. Rüssel, *Ceram. Int.*, 2019, **45**, 7580–7587.
68 C. Thieme, *J. Am. Ceram. Soc.*, 2021, **105**, 3544–3554.
69 C. J. Brinker and G. W. Scherer, *Sol-gel science: the physics and chemistry of sol-gel processing*, Academic Press, Boston, 1990.
70 S. Sakka, *Handbook of sol-gel science and technology: processing, characterization, and applications*, Kluwer Academic Publishers, Boston, 2005, vol. 3.

